

Angle-of-attack and Mach number effects on the aeroacoustics of an SD7003 airfoil at Reynolds number 60,000

International Journal of Aeroacoustics
2023, Vol. 22(1-2) 131–152

© The Author(s) 2023

Article reuse guidelines:

sagepub.com/journals-permissions

DOI: 10.1177/1475472X221150173

journals.sagepub.com/home/jae



Dhanush Vittal-Shenoy¹ , Romain Gojon¹, Thierry Jardin¹ and Marc C. Jacob² 

Abstract

The aeroacoustics of an SD7003 airfoil at Reynolds number 60,000 is investigated using Large Eddy Simulation. Five simulations are performed to study the effects of angle-of-attack and Mach number at fixed Reynolds number. For the three cases with angle-of-attack equal to 0° ($M = 0.1, 0.3$ and 0.6), a pure tonal noise associated with a 2D organisation of the flow is obtained. This flow topology is due to the establishment of a well known aeroacoustic feedback loop between the separation point on the suction side of the airfoil and the trailing edge. The occurrence of this loop is corroborated by the presence of a standing wave pattern with characteristic mode number in accordance with Panda's model. The main effect of the Mach number is to promote flow separation and hence increase separation length and mode number. In addition, the first harmonic and the sub-harmonic of the tone, observed in the far field acoustic spectrum, are found to be generated in the wake, presumably due to non-linear vortex interactions. For the two other angles-of-attack 4° and 8° at $M = 0.1$, the feedback loop does not establish and a Laminar Separation Bubble (LSB) is observed. When increasing the angle-of-attack, the LSB shrinks with earlier reattachment. For those two cases, far-field spectra are characterized by a low frequency associated with the breathing motion of the LSB and the reattachment point fluctuating in space. The frequency of this fluctuation depends on the curvature of the bubble. Far-field spectra are also characterized by a broadband trailing edge noise whose frequency range decreases with the angle-of-attack. Again, this evolution is found to depend on the curvature of the bubble which may promote a centrifugal instability in the separated shear layer.

Keywords

Aeroacoustics, airfoil noise, large eddy simulation

¹ISAE-Supaero, Université de Toulouse, Toulouse, France

²Ecole Centrale de Lyon, Laboratoire de Mécanique des Fluides et d'Acoustique, Ecully Cedex, France

Corresponding author:

Dhanush Vittal-Shenoy, Department of DAEP, ISAE-SUPAERO, 4 avenue Edouard Belin Toulouse 31056, France.

Email: dhanush.vittal-shenoy@isae-supaero.fr

Introduction

Recent applications for small unmanned air vehicles (UAVs) have been on the rise; from recreational to scientific usage, in civilian and military fields. In a large number of civilian applications UAVs are operated close to the populations and the noise regulations are accordingly expected to become more stringent. On the other hand, usage in a military context usually requires stealth UAVs. Finding ways to reduce UAV noise has thus become crucial and has fostered research on UAV noise sources these past few years.

The noise sources in UAVs are typically associated with the propulsion system, with a large contribution from the rotor. Rotor noise associated to high speed propellers and helicopters has been exhaustively studied since the 1930s, (Gutin;¹ Leverton and Taylor;² Lowson;³ Hanson,⁴ but small UAVs differ from helicopters in that they operate at much lower Reynolds numbers, typically 10^4 to 10^5 . In these regimes, the flow may remain laminar over significant portions of the blade, separate and face laminar-to-turbulent transition potentially leading to reattachment, which in the time average sense leads to the existence of laminar separation bubbles (LSB). Noise sources in these flow regimes are less explored with a limited amount of recent studies on low Reynolds number propellers such as experimental studies by Grande et al.⁵ and Gojon et al.⁶ and computational study by Romani et al.⁷ A first step towards their investigation relies on the analysis of noise sources on transitional airfoils (Moreau et al;⁸ Rozenberg et al;⁹ Golubev.¹⁰).

The noise produced by an isolated airfoil, usually referred to as airfoil self noise, can be described as the noise produced by the interaction of the airfoil's boundary layer and wake with itself. Various mechanisms at the origin of airfoil self noise can occur depending on operating conditions, typically defined by angle-of-attack, Reynolds number and Mach number.

One of the most characteristic feature was first evidenced by Paterson et al¹¹ with their experiments on symmetric NACA airfoils at relatively large Reynolds numbers. They found that for specific angles-of-attack, the sound spectra were dominated by discrete harmonics (tones) each scaling with $U_\infty^{0.8}$, where U_∞ was the freestream velocity. These tones were superimposed on a broadband hump, the maximum of which scaled with $U_\infty^{1.5}$. Thus the tone nearest to the hump maximum dominated the spectrum over a range of velocities and evolved with 0.8th power of the velocity until it was replaced by the next harmonic that underwent the same evolution. As a result, the dominant tone evolved as a combination of these two power laws in a ladder type structure: the ladder bars had the slope of the tones $U_\infty^{0.8}$ whereas the global slope of the ladder was that of the hump maximum $U_\infty^{1.5}$. Paterson related the hump frequency to 'natural' vortex shedding with $d \approx 2 \times \delta$, that is, the early wake width, δ being the BL thickness, but it did not explain the 'ladder-type' structure. In an effort to explain the 'ladder-type' pattern observed by Paterson et al,¹¹ Tam¹² proposed an aeroacoustic feedback loop mechanism where hydrodynamic instabilities grow along the airfoil, scattering at the trailing edge into acoustic waves that propagate upstream and further excite the aforementioned instabilities. A synthesis of the two approaches was proposed by Arbey & Bataille.¹³ A substantial amount of work was then conducted to clarify the feedback process experimentally (Yakhina,¹⁴ numerically (N'Guyen et al.¹⁵ and analytically (Yakhina et al.¹⁶ Despite some remaining questions, it can overall be understood that the aeroacoustic feedback loop acts as a frequency selection mechanism for the existing vortex shedding induced by the laminar separation bubble. That is, the presence of LSB and subsequent Kelvin-Helmoltz shear layer instabilities is a necessary condition for the occurrence of tonal noise. It was further demonstrated that the frequency selection process leads to the flow being highly coherent in the spanwise direction, i.e. with prominent quasi-two-dimensional structures.

Two-dimensional tonal coherence peaks were found to decrease as the separated shear layer delimiting the LSB reattaches closer to the leading edge. This typically occurs as the angle-of-attack is increased, leading to a reattached boundary layer that has increased time to transition to a fully turbulent state before reaching the trailing edge. As a consequence the flow may switch from tone-producing to no-tone-producing regimes and the scattering of smaller-scale turbulent structures at the trailing edge may become a dominant source of noise. The latter leads to a broadband noise usually referred to as trailing edge turbulent noise. Due to its predominance in a wide range of operating conditions, trailing edge turbulent noise has been widely studied and much attention has been given to the theoretical treatment of the underlying mechanisms, such as in Amiet¹⁷ and Howe¹⁸ theories, for example.

In addition to trailing edge tonal and broadband self noise, airfoil self noise may result from the unsteady surface pressure field due to the footprint of vortex structures. A notable example is the case of stalled flows where massive leading edge separation leads to both tonal and broadband noise at low frequencies.^{19,20}

The investigation on airfoil self noise has long relied upon experiments (e.g., Lately,^{11,13,21} together with the exponential growth in computational resources, numerical analysis helped gaining further insight into the aforementioned mechanisms (e.g., Yet,^{22,23} most numerical studies addressed the problem under a two-dimensional perspective which is a rather strong hypothesis even under operating conditions that lead to an aeroacoustic feedback loop and prominent tonal noise.^{10,24} On the other hand, previous studies have analyzed coupled Reynolds number and Mach number effects (by increasing the freestream velocity) and the role of Mach number at moderate Reynolds number is virtually unknown although it becomes highly relevant to small UAV noise where airfoils with small chord-length may operate at relatively high speeds. Therefore, the goal of the present study is to employ high-fidelity three-dimensional numerical simulations to assess the role of angle-of-attack and Mach number on the aeroacoustics of an SD7003 airfoil at a moderate Reynolds number of 60,000. First, the different regimes that occur at low Mach number when the angle-of-attack is varied, are characterized. Second, the role of the Mach number at low angle-of-attack and constant Reynolds number is brought up. The remainder of the paper is organized as follows: next section is dedicated to a description of the numerical approach undertaken in this research whereas the results are discussed in the following section, with an emphasis on the angle-of-attack influence and the Mach number effects. In the final section, the conclusions are drawn and suggestions for upcoming research are expressed.

Numerical Setup

The flow past an SD7003 airfoil at a chord-based Reynolds number of 60,000 is numerically solved using wall-resolved Large Eddy Simulations (LES). Simulations are performed with the massively parallel finite-volume solver IC3 which solves the compressible Navier-Stokes equations on unstructured grids. Here 4th order spatial and 3rd order Runge Kutta temporal schemes are chosen. The code has been previously described and successfully applied to a number of configurations,^{2,25} notably providing unique databases for high speed flows past airfoils. In the present study, the Vreman model 23 is used to model turbulent Sub-Grid Scales (SGS). Five wall-resolved Large Eddy Simulations have been performed. The angle-of-attack and the Mach number are varied whereas the Reynolds number is kept constant by changing the viscosity. For the five simulations, $t^* = 40$ convective times, based on the chord and the free stream velocity, are computed. The main characteristics are summarized in [Table 1](#).

The three dimensional computational domain is meshed using a C-type mesh topology as shown in Figure 1, with streamwise and vertical dimensions $-15C \leq x \leq 30C$ and $-15C \leq y \leq 15C$ respectively (where C is the chord length). It was verified that these dimensions ensure that the solution is unaffected by the domain boundaries. The spanwise extent is set to $0.2 C$, in line with previous results by Galbraith & Visbal,²⁶ Carton de Wiart & Hillewaert,²⁷ Turner & Kim.²⁰ For the cases $\alpha \neq 0$, when the flow is not affected by an aeroacoustic feedback loop that lead to a 2-D organisation of the flow, the spanwise extent has been checked by doing cross-correlation of velocity fluctuations in the turbulent boundary layer at $x/C = 0.8$.

The mesh is divided into three zones, as shown in Figure 1. Zone 1 in the vicinity of the airfoil is wall resolved in the sense that the cell size is $\Delta y^+ < 1$ in wall units at the airfoil surface. In addition, cells in this region have streamwise and spanwise dimensions $\Delta x^+ \sim \Delta z^+ \sim 10$. The mesh in the wake is adjusted according to the angle-of-attack. In Zone 2 the mesh is designed in such a way as to propagate acoustic waves at frequencies up to 2000 Hz into a region of $10C$ radius around the airfoil, with at least 10 grid points per wavelength. Zone 3 is a sponge zone used to dissipate vorticity, sound and entropy waves and to limit reflections at the far field boundaries. The total number of hexahedral cells is approximately 35 millions.

The computational time-step ensures that the Courant number based on both convective and acoustic speeds does not exceed unity.

No-slip, adiabatic boundary conditions are applied at the airfoil surface and periodic boundary conditions are used in the homogeneous spanwise direction. To avoid acoustic reflections at the inlet and on the upper and lower domain limits, soft free stream conditions are applied based on the Riemann invariants. At the outlet, pressure conditions are applied.

Table I. Characteristics of the five wall-resolved Large Eddy Simulations performed.

	Airfoil	Re	M	AoA	t^*
LES 1	SD7003	60,000	0.1	0°	40
LES 2	SD7003	60,000	0.1	4°	40
LES 3	SD7003	60,000	0.1	8°	40
LES 4	SD7003	60,000	0.3	0°	40
LES 5	SD7003	60,000	0.6	0°	40

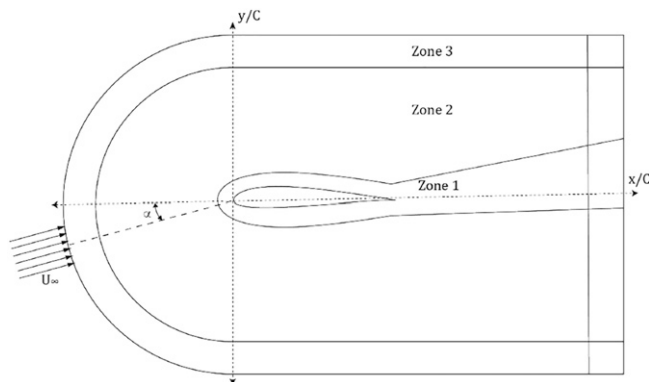


Figure 1. C-type mesh topology around SD7003 airfoil (not-to-scale).

To save computational time, the initial field is computed on a two-dimensional slice of the full 3D mesh and extruded into the spanwise direction.

The mesh resolution is first assessed using the Pope criterion $IQ_{\mathcal{K}}$, which represents the ratio between resolved turbulent kinetic energy and the sum of the resolved and the modeled turbulent kinetic energy, $IQ_{\mathcal{K}} = \mathcal{K}/(\mathcal{K} + \mathcal{K}_{SGS})$. The resolved turbulent kinetic energy is evaluated as $1/2(u_1'^2 + u_2'^2 + u_3'^2)$, where u_i' is the value of the velocity fluctuations in the i -th direction. The subgrid turbulent kinetic energy is estimated as $\mathcal{K}_{SGS} = (\nu_t/(C_M\Delta))^2$, where ν_t is the turbulent viscosity, C_M is Vreman constant (set to 0.069) and Δ is the cubic root of the cell volume. In general, according to Pope (Pope, S. B.²⁸ and Pope, S. B.,²⁹ page 558), a resolved LES must capture 80% of the turbulent kinetic energy. The probability density function (PDF) of the Pope index (not shown here for the sake of conciseness) indicates that the present mesh resolves more than 95% of the turbulent kinetic energy.

In addition, the spanwise and time-averaged pressure coefficients $C_p = 2(p - p_{\infty})/(\rho_{\infty}U_{\infty}^2)$, where p , p_{∞} , ρ_{∞} and U_{∞} are the airfoil mean surface pressure, the free stream static pressure, fluid density and velocity, respectively. The results obtained at Reynolds number 60,000, Mach number 0.1 and angles-of-attack $\alpha = 4^\circ$ and 8° are assessed against numerical,^{26,27,30,31} and experimental³² results from the literature and plotted on Figure 2. The present results are in good agreement with the numerical results from literature. Discrepancies are observed with experimental results,³² due to the high sensitivity of the separation bubble with respect to the environment (blockage, wing span, freestream turbulent intensity, wing surface roughness) (e.g. Tank et al 2017.³³) In particular, freestream turbulent intensity is absent in numerical simulations and inherent to wind tunnel experiments. The C_p profiles exhibit the typical features of a laminar separation bubble, that is, a low plateau within the bubble (slightly decreasing in the 8° case followed by a quick pressure recovery as the separated shear layer reattaches. This will be further discussed in the next section.

Accordingly, the time-averaged lift C_l and drag C_d coefficients compare well with numerical data from the literature, with $C_l = 2L/(\rho_{\infty}CSU_{\infty}^2)$ and $C_d = 2D/(\rho_{\infty}CSU_{\infty}^2)$, where S , L and D are the airfoil span length, and the lift and drag forces experienced by the airfoil, respectively. Data obtained in various studies including the present work for $\alpha = 4^\circ$ and $\alpha = 8^\circ$ are reported in Table 2.

Note that statistics are computed over a time window corresponding to at least 15 convective times $t^* = tU_{\infty}/C$, where t is the time.

Results

Effect of angle-of-attack

Numerical simulations are performed for angles-of-attack 0° , 4° and 8° at Reynolds number 60,000 and Mach number 0.1. Figure 3 shows instantaneous isosurfaces of the Q-criterion for the respective angles-of-attack, highlighting the onset and growth of instabilities as well as the development of turbulence in the 4° and 8° cases. Indeed the flow structure indicates that the flow remains 2D and coherent for $\alpha = 0^\circ$ while three dimensional structures are observed shortly after the onset of transition for 4° and 8° .

Time averaged lift and drag coefficients are given in Table 3. It can be seen that both C_l and C_d coefficients increase with the angle-of-attack, as expected.

To further examine the development of flow structures on the airfoil, the streamwise velocity profiles averaged both in time and in the spanwise direction, are plotted every 0.1 C on the suction side of the airfoil in Figure 4, together with the displacement thickness δ^* and momentum thickness θ . Velocity profiles are obtained along the direction normal to the surface.

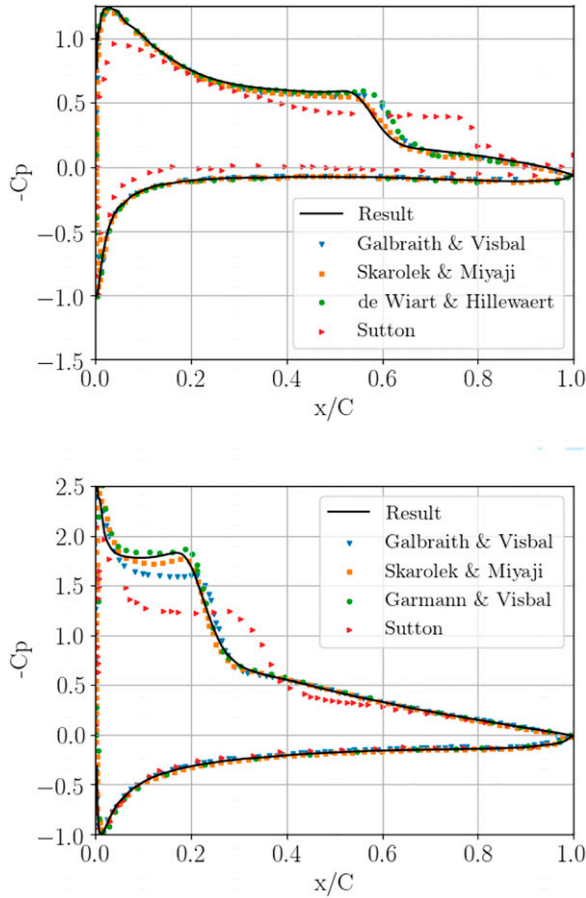


Figure 2. C_p distribution for $Re = 60,000$, $M = 0.1$, $\alpha = 4^\circ$ (top) and 8° (bottom). Comparison with previous numerical and experimental results from the literature.

Table 2. Time averaged C_l and C_d for $Re = 60,000$, and $M = 0.1$. Comparison with previous numerical and experimental results from the literature for $\alpha = 4^\circ$ and $\alpha = 8^\circ$.

Angle-of-attack	4°		8°	
	C_l	C_d	C_l	C_d
Present	0.59	0.021	0.93	0.046
Galbraith & Visbal ²⁶	0.59	0.021	0.923	0.045
Skarolek & Miyaji ³⁰	0.589	0.019	0.9331	0.0389
Carton de Wiert & Hillewaert ²⁷	0.607	0.020	—	—
Garmann & Visbal ³¹	—	—	0.9696	0.0391
Sutton ³²	0.49	—	0.94	—

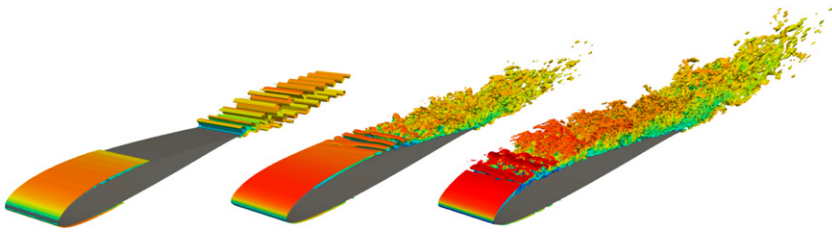


Figure 3. Instantaneous isosurfaces of Q-criterion coloured with local Mach number for angles-of-attack $\alpha = 0^\circ, 4^\circ$ and 8° (from left to right) ($Re = 60,000$ and $M = 0.1$).

Table 3. Time averaged lift and drag coefficients.

Angle-of-attack	C_l	C_d
0°	0.070	0.015
4°	0.59	0.021
8°	0.93	0.046

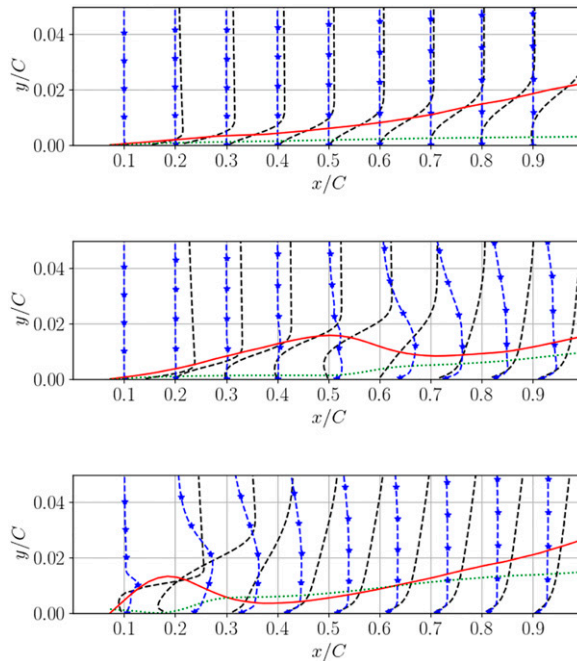


Figure 4. Boundary layer profiles obtained for $\alpha = 0^\circ, 4^\circ$ and 8° (from top to bottom). Spanwise- and time-averaged mean (black) and rms (blue) velocity profiles along the surface normal direction overlaid with displacement thickness δ^* (plain red line) and momentum thickness θ (dotted green line).

In the $\alpha = 0^\circ$ case, a small flow reversal occurs near the trailing edge (at $x/C \sim 0.8$), which is in line with the flow separation and subsequent formation of 2D roll-ups previously detected in Figure 3. Accordingly, the increase in displacement thickness is enhanced near the trailing edge while the increase in momentum thickness remains approximately almost constant, which indicates that the friction increase remains limited. This can be explained by noticing that the reverse velocity is much smaller than the free stream velocity and resulting in a reduced gradient at the wall. In the $\alpha = 4^\circ$ case, flow reversal is observed for velocity profiles located at $x/C = 0.3, 0.4$ and 0.5 . That is, the flow separates earlier than in the $\alpha = 0^\circ$ case and then reattaches: the flow reversal confirms the presence of a recirculation bubble already identified on the C_p plot. The latter suggests that the reattachment occurs at $x/C \sim 0.5 - 0.55$. The displacement thickness δ^* increases with x inside the bubble and decreases beyond $x/C = 0.5$ as the flow reattaches, which is a trace of the boundary layer deviation due to the bubble. Downstream of $x/C = 0.75$, δ^* increases again together with the development of the reattached boundary layer, which is consistent with the formation of three-dimensional, small scale structures previously observed in Figure 3. The momentum thickness θ does not significantly increase inside the bubble (due to the near stagnant nature of the flow) but increases downstream of it, due to the laminar-to-turbulent transition of the boundary layer visible in the rms streamwise velocity profiles and already observed in Figure 3. In the $\alpha = 8^\circ$ case flow reversal occurs even closer to the leading edge but over a much shorter portion of the airfoil. That is, the time-averaged flow reattaches at $x/C = 0.3$ leaving a longer downstream distance along the airfoil for θ and δ^* to increase before the flow reaches the trailing edge.

The shrinking of the LSB with α is in line with C_p distributions previously observed in Figure 2.

Figure 5 shows the instantaneous pressure fluctuation field for the three test cases. It can be clearly seen from the regularly spaced sharp wave fronts, that in the $\alpha = 0^\circ$ case, the airfoil radiates sound at a clearly dominant frequency (i.e. tonal noise) while the acoustic fields corresponding to the $\alpha = 4^\circ$ and $\alpha = 8^\circ$ cases are more complex and suggest a broadband radiation: the wave fronts tend to smear out at increasing angle-of-attack. However the distance between the main wave fronts is of the same order as in the 0° case. Thus the broadband noise is expected to radiate around a preferred frequency that is of the same order as the tonal frequency from the 0° case. The main directivity is that of a compact dipole in the cross-stream direction. Moreover a slight upstream wave front tightening reveals a small Doppler effect due to the convection. The wavelength of the acoustic waves observed at $\alpha = 0^\circ$ is found to be $1.48 C$. These snapshots also show that acoustic reflections are properly avoided with the present numerical setup.

The power spectral density of the pressure fluctuations obtained on the upper surface (suction side) of the airfoil at various chordwise locations is shown in Figure 6 for the three test cases.

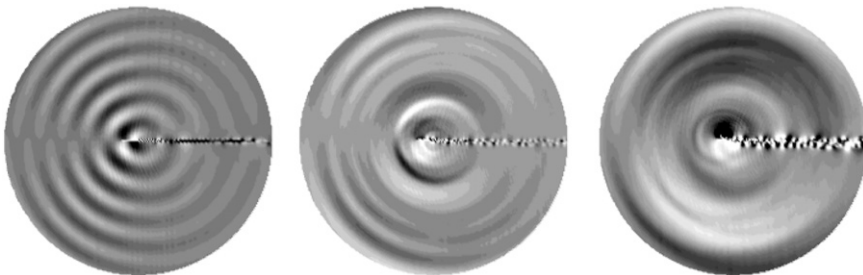


Figure 5. Instantaneous pressure fluctuation field (ranging between ± 1 Pa) obtained for $\alpha = 0^\circ, 4^\circ$ and 8° (from left to right).

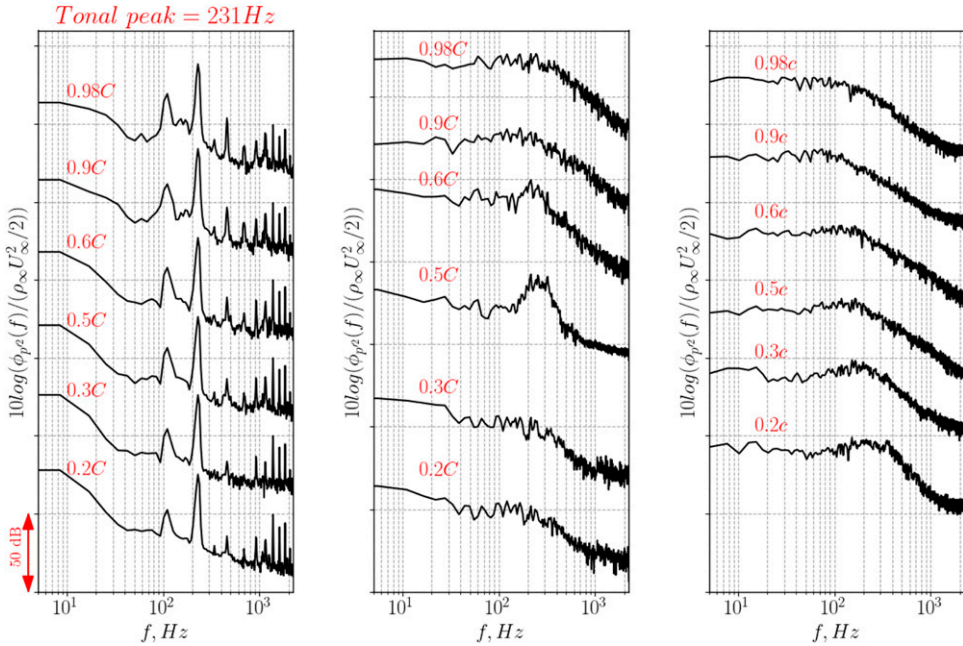


Figure 6. Power spectral densities (PSD) of pressure fluctuations obtained at locations 0.2c, 0.3c, 0.5c, 0.6c, 0.9c and 0.98c (with an offset of 50 dB between each) for $\alpha = 0^\circ$, 4° and 8° (from left to right).

Surface pressure fluctuations are acquired at a sampling frequency of 4200 Hz during 1.61s corresponding to 50 convective times. Power Spectral Density are obtained from time signals by computing the fast Fourier transform (FFT) with a Hanning window applied on 2 segments, without overlap. The frequency resolution is $\Delta f = 1.25$ Hz. Note that the curves obtained at different locations are offset by 50 dB for the sake of clarity. At $\alpha = 0^\circ$, a prominent peak is observed at 231 Hz, corresponding to the 1.48 C wavelength previously observed on Figure 5, for all chordwise locations. This frequency corresponds to the trailing edge vortex shedding frequency, which explains that the peak amplitude grows towards the trailing edge. The spectra are also characterized by sub- and super-harmonics. The sub-harmonics reveal a non-linear interaction in the source mechanism, that could be, for instance, related to vortex merger in the near wake. Both sub- and super-harmonics grow towards the trailing edge, which is consistent with the vortex formation in this region. At $\alpha = 4^\circ$ there is no evidence of narrow peaks. Instead of tones, a relatively broad peak is observed at 0.5 C and 0.6 C , around 231 Hz as already inferred from the snapshots of Figure 5. The 0.5 C location is found to be within the separation bubble, where the displacement thickness is maximal (Figure 4). Although the exact mechanism is unclear at this point, it seems reasonable to relate the onset of vortex formation to bubble oscillations. These oscillations are influenced by the rapid onset of turbulence in this region (see Figure 3) and are therefore rapidly smeared out into the downstream direction. The PSD of the broadband wall pressure fluctuations reaches much higher amplitudes than those observed at $\alpha = 0^\circ$, for all chordwise locations. At $\alpha = 8^\circ$, rather than a broad peak, a hump is observed at 0.2 C and 0.3 C , which here again corresponds to the location of the separation bubble and of the onset of turbulence, 0.2 C being the location where the displacement

thickness is maximal. The downstream increase of the wall pressure amplitude mentioned for the $\alpha = 4^\circ$ case, can also be seen at this angle-of-attack, where it is much more pronounced.

Some of the features of the wall pressure field can also be found in the far field, as shown in Figure 7 in which the sound pressure levels obtained at $(0.5 C, 8C)$ corresponding to an angle of 90° to the chord, are plotted for all angles-of-attack. Overall, relatively narrow peaks are observed at $\alpha = 0^\circ$ while larger amplitude broadband noise is observed at $\alpha = 4^\circ$ and 8° . More precisely, a number of small peaks arise from a broad hump ($20 - 300$ Hz) in the $\alpha = 4^\circ$ case. In the $\alpha = 8^\circ$ case, the highest values are reached in the frequency $10 - 150$ Hz with a low frequency end of the spectrum that remains flat with a few small jigsaws. Individual peaks are hardly recognisable, except for a peak at a frequency close to the aforementioned sub-harmonic. In particular, the hump at $20 - 30\%$ chord seems not to radiate very efficiently into the far field.

In an effort to identify the different noise sources for all three cases, the time cross-correlation between the pressure fluctuations along the x -axis on the airfoil surface or the wake $p_s(x, t)$ and the far acoustic pressure field $p_a(t+\Delta t)$ is computed, Δt being the correlation time between the two signals. The pressure in the far-field is recorded at a fixed position $(0.5c, 8c)$. All signals are filtered by a $\Delta f = 5$ Hz wide band-pass filter for frequencies ranging from 2 Hz to 500 Hz. The cross-correlation between the two variables at a given position x of the filtered aerodynamic pressure $p_s(x, t, f, \Delta f)$, a given correlation time Δt and a given frequency f is computed as:

$$C_{pp}(x, \Delta t, f) = \frac{S_{p_a(t+\Delta t, f)p_s(x, t, f)}}{\sigma_{p_a(t, f)}\sigma_{p_s(x, t, f)}} \quad (1)$$

where S is the co-variance and σ is the standard deviation obtained from a time average. The maximum value for all correlation times of C_{pp} is computed at a given filter width Δf , for all frequencies f and aerodynamic probe positions x/C . The result is mapped for the 3 cases on Figure 8.

For $\alpha = 0^\circ$, in the airfoil region ($x < C$), the frequency versus chordwise location map exhibits simple patterns, with strong correlations observed as straight horizontal bands. Strongest correlations appear around 231 Hz, in line with previous observations about Figures 5–7. It is also worth noting that the correlation is almost uniform along the airfoil as this suggests that the vortical structures shed by the airfoil are coherent with instabilities developing along the airfoil. Interestingly, in the wake region ($x > C$), maximum correlations for the first sub-harmonic and the first super-harmonic are observed at $x \approx 2.5 C$ and close to the trailing edge, respectively. These tones are also visible in the far field noise spectrum (see Figure 7). This result corroborates the direct analysis of the wall pressure spectra and suggests that the sub-harmonic frequency is associated to non-linear vortex interactions in the wake. The correlation plot also shows that in this pseudo-laminar case, the

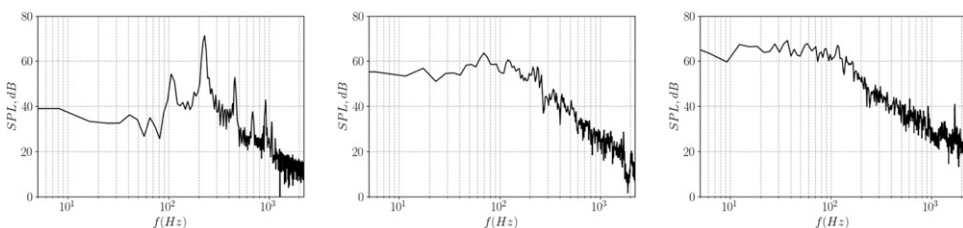


Figure 7. Far-field noise spectra obtained at $(0.5 C, 8C)$ from the airfoil for $\alpha = 0^\circ, 4^\circ$ and 8° (from left to right).

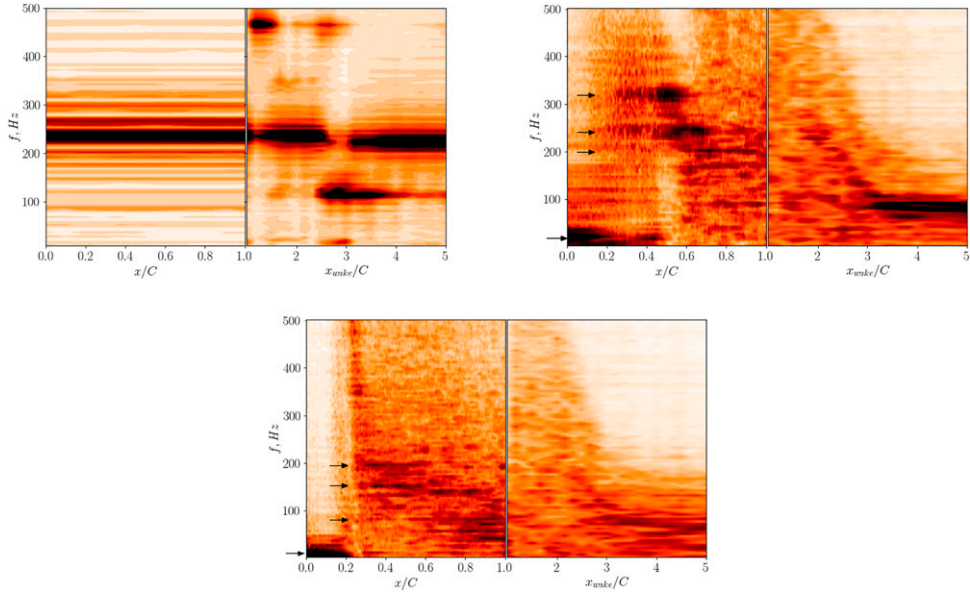


Figure 8. Maximum value of cross correlation C_{pp} of surface pressure to the pressure recorded in the near-field at (0.5c, 1.5c) mapped along frequency for $\alpha = 0^\circ$, 4° and 8° (from left to right). Arrows indicate regions of strong correlation.

shed vortices remain coherent far down the wake. Similar observations were made on a subcritical cylinder wake in the case of a rod-airfoil interaction (Jacob et al.,³⁴ Boudet et al.³⁵)

In the airfoil region, complex correlation patterns are observed for $\alpha = 4^\circ$ and 8° . At $\alpha = 4^\circ$, strongest correlations are observed at low frequencies (9 Hz) in the vicinity of the leading edge and at higher frequencies (around 195 ± 5 , 231 ± 20 and 310 ± 20 Hz) near $x/C \approx 0.5$ where the displacement thickness was found to be maximum. Please note that for 9 Hz, the total simulation time corresponds to about 20 periods, which is sufficient to have a converged cross-correlations. These frequencies that are actually frequency bands, are in the hump of the associated wall pressure spectra. The strong correlation patterns are indicated in Figure 8 with black arrows. It is also remarkable that correlations at frequencies between approximately 50 Hz and 200 Hz are very weak within the LSB, around $x/C \approx 0.5$ but the sub-harmonic frequency appears about 2 chords downstream of the airfoil, which is quite close to the $\alpha = 0^\circ$ case. This is also observed at $\alpha = 8^\circ$ where correlations within the LSB, from $x/C = 0$ to $x/C \approx 0.25$, have non-negligible amplitudes only at low frequencies. In this case, strongest correlations are observed at low frequencies (18 Hz) in the vicinity of the leading edge and at higher frequencies (around 90, 160 and 185 Hz) near ($x/C = 0.25$) and downstream of the reattachment point. Here again, high amplitude patterns can be found at frequencies around 100 Hz in the wake for $x/C > 2.5$: however it should be noted that these are less intense than for smaller angles-of-attack as the flow experiences higher turbulence levels with increased mixing.

To further analyse the pressure field at midspan, the Spectral POD (SPOD) method has been used. The SPOD has been recently proposed as an additional tool to characterize the main structures of a turbulent flow. The SPOD method relies on discrete Fourier transform (DFT) and POD methods to extract the main energetic structures and their characteristic frequency in the flow field. The

SPOD algorithm used here rely on the Welch formulation introduced by Towne et al.³⁶ and Schmidt and Colonius.³⁷ For the present study, 1600 2D pressure snapshots are used. The dataset is partitioned into smaller overlapping blocks, each block representing an ensemble realization of the flow. It corresponds to a splitting of the initial matrix into 3 blocks with 50% overlapping corresponding to 800 snapshots by block. Pressure fluctuations SPOD1 temporal functions obtained in the midspan cross-section are displayed in Figure 9. We focus on the prominently correlated frequencies for $\alpha = 8^\circ$ at 18 Hz and 185 Hz, which have been identified as frequencies with strong correlations in Figure 8. It can be seen that the high frequency mode is characterized by large amplitude packets originating in the separated shear layer and presumably advecting downstream. This suggests the onset of shear layer Kelvin-Helmholtz type instability and the subsequent formation of large scale spanwise structures around $x/C = 0.2$, i.e. around maximum displacement thickness, that shed from the LSB.^{38,39} The low frequency mode is characterized by large amplitudes clustered on both sides of the of the reattachment point, which seems to be between $x/C = 0.2$ and 0.3 according to Figure 4. This result suggests that this frequency is due to the streamwise motion of the reattachment point in time, and thus to the breathing motion of the bubble.

To further analyze this low frequency motion, both separation ($C_f = 2\tau/(\rho U_{inf}^2) = 0$ and $\partial C_f/\partial x < 0$) and reattachment ($C_f = 0$ and $\partial C_f/\partial x > 0$) points are tracked in time. Time evolution of those two points are given in Figure 10. While the motion of the separation point is found to be very limited, that of the reattachment point exhibits relatively strong unsteadiness at low frequencies. Specifically, by applying a Fourier transform to the reattachment point time evolution, cases with $\alpha = 4^\circ$ and $\alpha = 8^\circ$ are characterized by frequencies around 9 Hz and 18 Hz, respectively. The

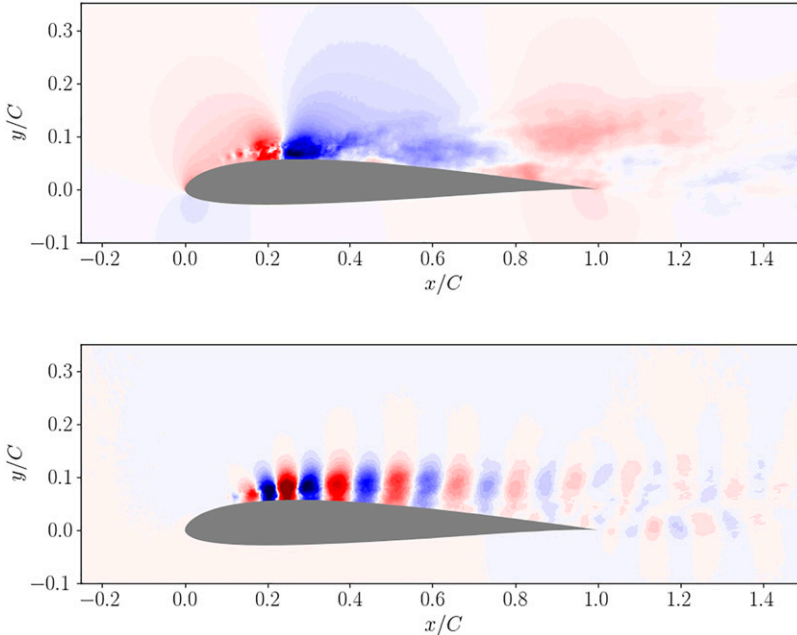


Figure 9. Pressure fluctuations SPOD1 temporal functions at prominently correlated frequencies 18 Hz (top) and 185 Hz (bottom) for $\alpha = 8^\circ$.

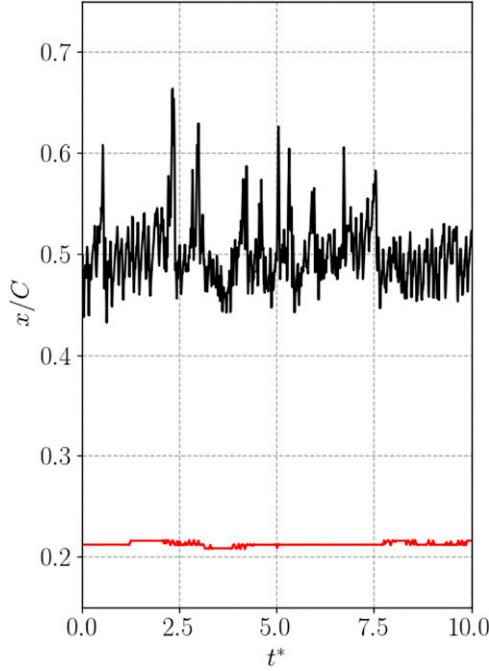


Figure 10. Time evolution of the separation (red) and reattachment (black) points for $\alpha = 4^\circ$.

occurrence of this low-frequency motion resembles ‘breathing’ or ‘flapping’ modes observed under favourable conditions on turbulent separation bubbles (e.g., Wu et al 2020.⁴⁰) The higher frequency for the case $\alpha = 8^\circ$ compared to the case $\alpha = 4^\circ$ is consistent with a smaller characteristic length scale (i.e. separation length) of the separation bubble (previously shown in Figures 2 and 4).

Finally, the isolines of Rayleigh discriminant ϕ are plotted in Figure 11 for the $\alpha = 4^\circ$ and 8° cases, together with contours of turbulent kinetic energy. ϕ is computed from spanwise- and time-averaged quantities as:

$$\phi(x, y) = \frac{2U\omega}{R} \quad (2)$$

where, $U(x, y)$ is the modulus of velocity, $\omega(x, y)$ the vorticity and R the local algebraic curvature $R = U^3/(ua_y - va_x)$, with (u, v) the components of the velocity field and (a_x, a_y) those of the convective acceleration. The $\phi = 0$ isolines delimit regions of negative ϕ where a centrifugal instability is likely to occur. Overall, three potentially unstable regions are observed. Region I can be attributed to the geometric curvature of the leading edge. Region II pertains to the reattachment of the bubble. Region III can be correlated with the occurrence of vortex shedding. The relative strength of the curvature with respect to the viscous effects can be quantified using the Görtler number:

$$G = \frac{U\delta^{3/2}}{\nu R^{1/2}} \quad (3)$$

where δ is the boundary layer thickness in the region considered and ν the kinematic viscosity of the fluid. The Görtler numbers for cases with $\alpha = 4^\circ$ and 8° are computed in region II where centrifugal instability at the reattachment point may drive the dynamics of the LSB. The value obtained for $\alpha = 8^\circ$ (≈ 150) exceeds that obtained for $\alpha = 4^\circ$ (≈ 50), which is in line with the lower frequency range of the radiated noise, passing from 20 – 300 Hz to 10 – 150 Hz when the angle-of-attack increases, as previously shown by Viaro & Ricco,⁴¹ for example. Therefore, while the $\alpha = 4^\circ$ and 8° cases yield significant high frequency trailing edge broadband noise with respect to the $\alpha = 0^\circ$ case, they are also characterized by low frequency noise that results from the dynamics of the LSB.

Effect of Mach number

Building on the previous analysis, we now investigate the effect of Mach number at $\alpha = 0^\circ$ and $Re = 60,000$. Figure 12 shows instantaneous isosurfaces of Q-criterion obtained for Mach numbers 0.1, 0.3 and 0.6. It can be observed that flow separation occurs closer to the leading edge as M increases. Yet, in all cases, the flow remains prominently two-dimensional over the airfoil and only transitions to smaller scale, three-dimensional structures in the wake for $M = 0.3$ and 0.6. This change in flow topology with Mach number corroborates previous observations by Désert et al⁴² where it was

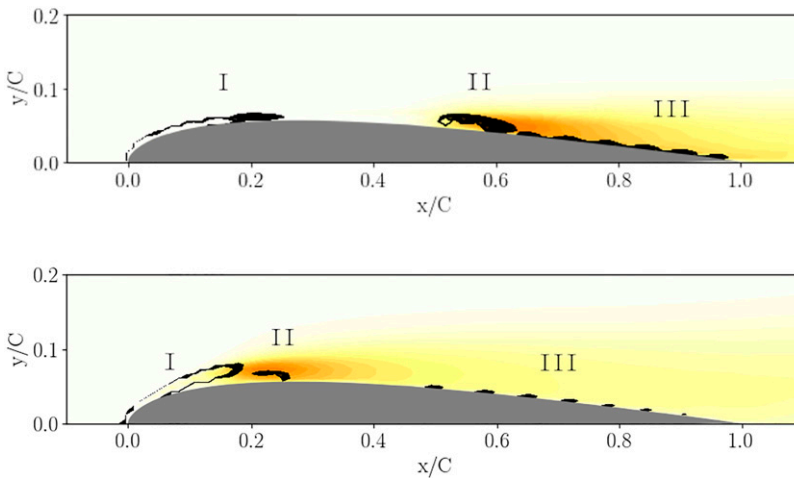


Figure 11. Isolines of zero Rayleigh discriminant (black) superimposed to contours of turbulent kinetic energy for $\alpha = 4^\circ$ (top) and 8° (bottom).

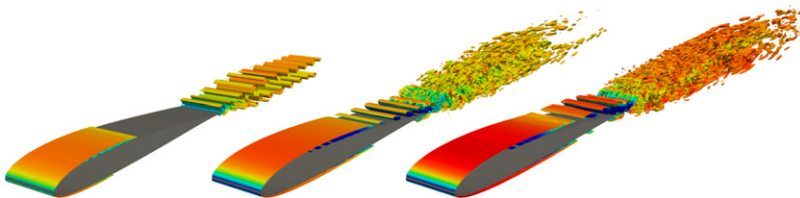


Figure 12. Instantaneous isosurfaces of Q-criterion coloured with local Mach number for Mach numbers 0.1, 0.3 and 0.6 (from left to right) ($Re = 60,000$ and $\alpha = 0^\circ$).

found that the separation point on a two-dimensional cambered airfoil at Reynolds number 3000 moves upstream with increasing Mach number.

Time averaged lift and drag coefficients are given in Table 4. At such angle-of-attack aerodynamic forces are weak and the influence of Mach number is not significant despite non-negligible changes in flow topology. It is worth noting though that, as expected, a larger change is observed from $M = 0.3$ to 0.6 than from $M = 0.1$ to 0.3 .

The increase in flow separation length is further illustrated in Figure 13 which plots the corresponding boundary layer profiles. Similarly to Figure 4, displacement and momentum thicknesses are superimposed to streamwise velocity profiles obtained along the normal surface direction every $x/C = 0.1$. Overall, it can be observed that the displacement thickness increases with increasing Mach number, together with the larger separation length. Conversely, the momentum thickness remains small with the absence of laminar-to-turbulent transition, and decreases with increasing

Table 4. Time averaged lift and drag coefficients.

Mach number	C_l	C_d
0.1	0.070	0.015
0.3	0.086	0.016
0.6	0.036	0.019

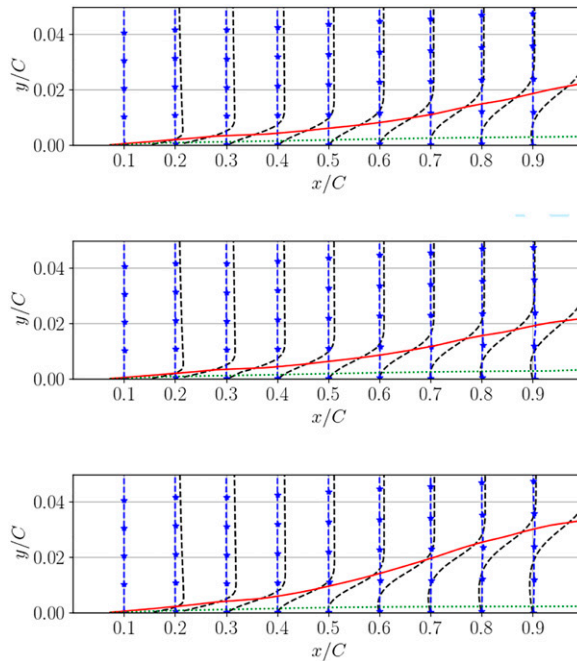


Figure 13. Boundary layer profiles obtained for $M = 0.1, 0.3$ and 0.6 (from top to bottom). Spanwise- and time-averaged streamwise mean (black) and rms (blue) velocity profiles along the surface normal direction overlaid with displacement thickness δ^* (plain red line) and momentum thickness θ (dotted green line).

Mach number. Accordingly with the absence of laminar-to-turbulent transition, the separated shear layer does not reattach prior to the trailing edge. This also echoes previous results by Munday et al⁴³ and Désert et al⁴² who highlighted an elongation of the laminar separated shear layer with increasing Mach number.

Figure 14 shows the instantaneous pressure fluctuation field for the three cases. As expected from the predominantly two-dimensional flow structure observed in Figure 12, all cases exhibit a clear dominant acoustic frequency that increases with Mach number. A clear Doppler effect with an upstream wave front tightening is observed, notably for $M = 0.3$ and 0.6 . In order to not be affected by this effect, the wavelength of the acoustic waves along the direction perpendicular to the flow are measured. Values of $1.48 C$, $0.74 C$, and $0.40 C$ are found for Mach number 0.1 , 0.3 and 0.6 respectively.

Dominant frequencies can further be identified on the power spectral density of pressure signals obtained from the upper surface of the airfoil. Figure 15 shows a number of tonal or quasi-tonal peaks: besides the dominant peaks, sub- and super-harmonic peaks tend to vanish as the Mach number increases, which is consistent with the increasingly turbulent nature of wake. The dominant frequencies are due to narrow peaks at 231 Hz and 462 Hz for $M = 0.1$ and $M = 0.3$ cases, respectively and to a relatively broad peak at 851 Hz for the $M = 0.6$ case. The dominant frequencies correspond to the wavelengths observed earlier in Figure 14. Moreover, these frequencies are found to scale with $U_\infty^{1.14}$, which is in line with the ‘ladder type’ pattern experimentally observed by Paterson et al¹¹ in the frequency versus freestream velocity map. As previously introduced, the ‘ladder type’ pattern results from the frequency selection process pertaining to the occurrence of an

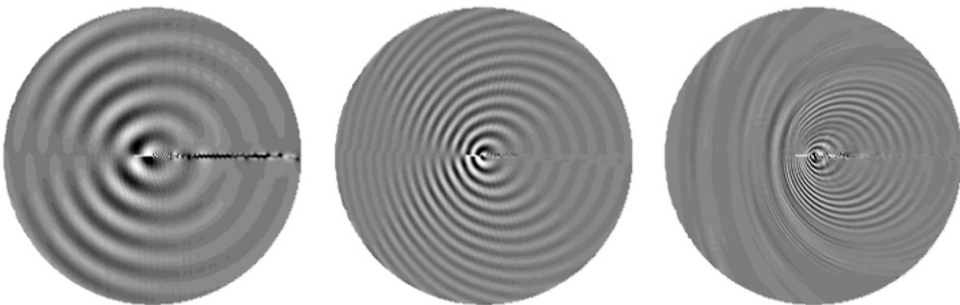


Figure 14. Instantaneous pressure fluctuation field obtained for $M = 0.1, 0.3$ and 0.6 (from left to right), with contours ranging between $\pm 1 \text{ Pa}$, $\pm 100 \text{ Pa}$ and $\pm 250 \text{ Pa}$, respectively.

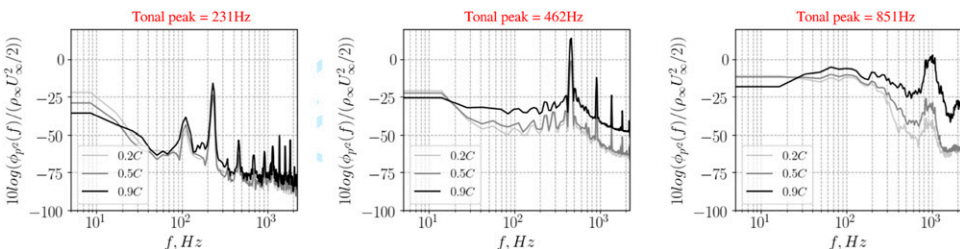


Figure 15. Power spectral densities (PSD) of pressure fluctuations obtained at locations $0.2c, 0.5c$, and $0.9c$ for $M = 0.1, 0.3$ and 0.6 (from left to right).

aeroacoustic feedback loop. The latter can be characterized by the existence of a ‘standing wave’ resulting from the propagation of two pressure waves with opposite velocities and same frequency. Panda et al⁴⁴ observed this phenomenon in jet flows where downstream waves are of hydrodynamic nature while upstream waves are of acoustic nature, similarly to what is observed on the present airfoil case. A simple model can be derived from the work of Panda et al⁴⁴ to predict the frequency of the feedback loop, on which the vortex shedding frequency locks on. It reads:

$$f = \frac{N}{L \left(\frac{1}{a_0 - U_\infty} + \frac{1}{U_c} \right)} \quad (4)$$

where f is the frequency of the aeroacoustic feedback loop, U_∞ is the freestream velocity, U_c is the mean convection velocity of the vortical structures induced by flow separation, L is the length where the feedback loop is established (i.e., from the separation point to the trailing edge) and N is the number of nodes of the standing wave. Physically, N indicates the number of times the feedback mechanism occurs during the period of the loop. U_c is computed following two approaches. The first one considers cross-correlations of pressure fluctuations at the airfoil upper surface, from the separation point to the trailing edge. The second one considers local velocities where turbulent kinetic energy is found to be maximum (also restricted to the region extending from the separation point to the trailing edge). Both approaches yield similar results.

N can be visualized by displaying the gradient of the amplitude of the Fourier modes corresponding to the tonal frequency, obtained from the fast Fourier transform of pressure signals at the

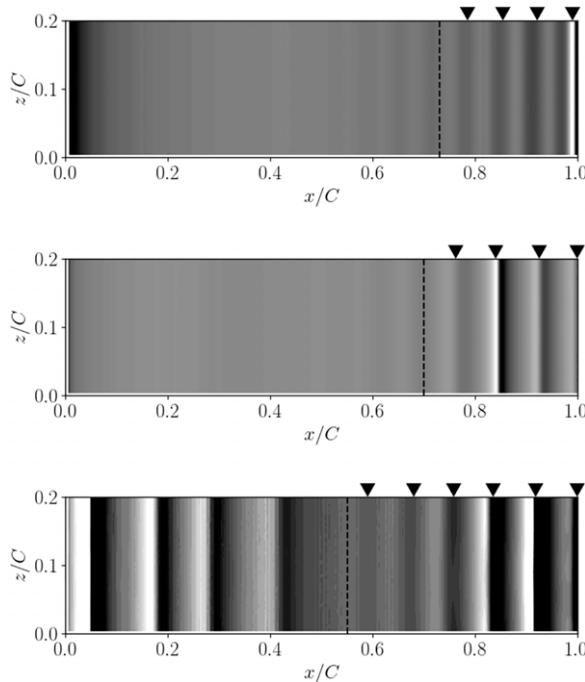


Figure 16. Gradient of the amplitude of the surface pressure Fourier modes corresponding to the tonal frequency, for $M = 0.1, 0.3$ and 0.6 (from top to bottom). The dotted lines indicate the chordwise location of flow separation.

Table 5. Comparison between tonal frequencies obtained from pressure spectra and from the model.

	f spectra, Hz	Uc	N	L	f model, Hz
M = 0.1	231	0.588 U _∞	4	0.37c	228
M = 0.3	456	0.495 U _∞	4	0.41c	460
M = 0.6	851	0.52 U _∞	6	0.46c	853

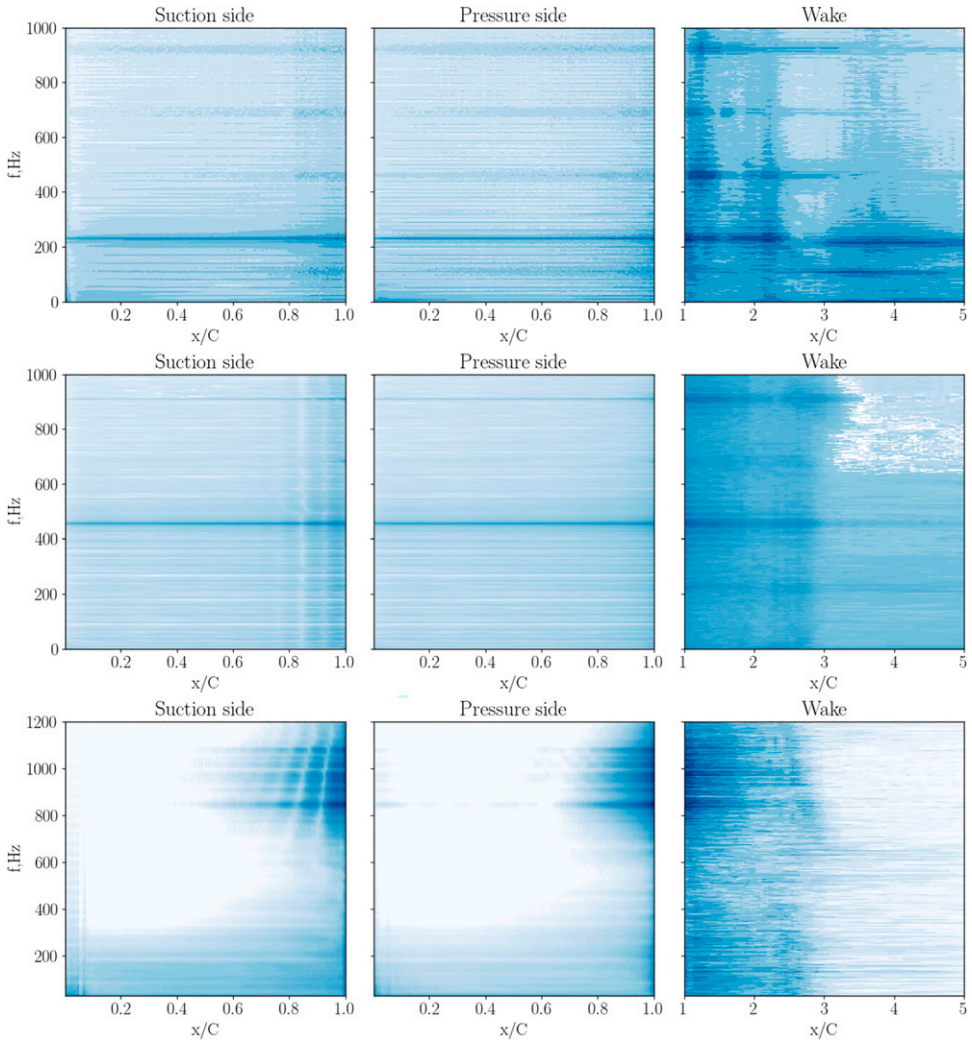


Figure 17. Amplitude versus frequency maps on the suction and pressure sides of the airfoil and in the wake for $\alpha = 0^\circ$ at Mach number M = 0.1, 0.3 and 0.6.

airfoil upper surface. Figure 16 shows that the $M = 0.1, 0.3$ and 0.6 cases are characterized by $N = 4, 4$ and 6 , respectively. Note that the dashed line represents the chordwise location of the separation point.

Values of N , U_c and L are reported in Table 5 together with the frequency obtained from the model and from spectra in Figure 15. It is found that frequencies obtained from the model and directly from spectra are in relatively good agreement, which supports the idea that the flow dynamics is driven by the occurrence of an aeroacoustic feedback loop in all three cases.

Finally, the amplitude versus frequency maps of the Fourier modes obtained from pressure signals on both upper and lower surfaces of the airfoil and in the wake are displayed in Figure 17. First, it can be observed that the primary tone is clearly visible on both upper and lower surfaces, over the whole chord length in the $M = 0.1$ and 0.3 cases but mostly beyond midchord in the $M = 0.6$ case. Second, while super-harmonics are also visible at $M = 0.1$ and 0.3 on the surfaces of the airfoil, they appear more clearly in the wake. This is further the case for the sub-harmonic at $M = 0.1$. This suggests that sub- and super-harmonics originate in the wake and are associated with the dynamics of wake vortices. In particular, the sub-harmonic appears to coincide with the wake pattern transitioning from a ‘single-row’ to a ‘double-row’ vortex street (e.g. Désert 2019.⁴²) It can be noted that there is no clear evidence of sub-harmonics at $M = 0.3$ and 0.6 , together with the transition of the wake into small scale three-dimensional structures.

Conclusion

The aeroacoustics of an SD007 airfoil at low Reynolds number ($Re = 60,000$) is investigated using Large Eddy Simulation. Five simulations are performed to study the effect of the angle-of-attack and the effect of the Mach number at fixed Reynolds number.

The effect of the angle-of-attack α at a fixed Mach number 0.1 is first analyzed. Simulations at $\alpha = 0^\circ, 4^\circ$ and 8° are performed. Both time averaged lift and drag coefficients increase with the angle-of-attack, together with a displacement of the boundary layer separation point towards the leading edge. For the $\alpha = 0^\circ$ case, a pure tonal noise associated with a 2D organisation of the flow is observed. This flow topology results from the establishment of a well known aeroacoustic feedback loop. The first harmonic and the sub-harmonic of this tone, observed in the far field acoustic spectrum, are generated in the wake and presumably result from non-linear vortex interactions. For the two other angles-of-attack $\alpha = 4^\circ$ and 8° , the feedback loop does not establish and a Laminar Separation Bubble (LSB) is observed. When increasing the angle-of-attack, the LSB shrinks with a reattachment point passing from $x/C \sim 0.5 - 0.55$ to $x/C \sim 0.3$. Concomitantly, the low frequency that characterizes far-field spectra passes from 9 to 18 Hz. Those frequencies are found to be associated with the breathing motion of the LSB and the reattachment point fluctuating in space. The frequency of this fluctuation depends on the curvature of the bubble. Thus, the higher frequency obtained for $\alpha = 8^\circ$ compared to $\alpha = 4^\circ$ is consistent with a smaller characteristic length scale (i.e. separation length) of the separation bubble. Far-field spectra are also characterized by a broadband trailing edge noise passing from $20 - 300$ Hz to $10 - 150$ Hz when the angle-of-attack increases from $\alpha = 4^\circ$ to $\alpha = 8^\circ$. This evolution appears related to the curvature of the bubble which promotes centrifugal instability in the separated shear layer, potentially leading to Görtler type instability vortex shedding. By increasing the curvature, the Görtler number increases, leading to a decrease of the vortex shedding frequencies.

Mach number effect is then studied at a fixed angle-of-attack of 0° with simulations at $M = 0.1, 0.3$ and 0.6 . When increasing the Mach number, the boundary layer is found to separate closer to the leading edge. Yet, although this increases the time for the separated shear layer to transition to a

turbulent state and potentially reattach, the shear layer remains fully separated. These changes in flow topology with Mach number do not yield significant changes in time averaged lift and drag coefficients which are weak at this angle-of-attack. For all cases, a tonal noise component is found to dominate. This noise component is due to an aeroacoustic feedback loop establishing between the separation point on the suction side of the airfoil and the trailing edge. The presence of this loop leads to the observation of a standing wave pattern, characterized by a mode number that, together with the spatial extent of the separated region, matches with Panda's model.

Acknowledgements

The authors are grateful to GENCI-IDRIS, GENCI-CINES (Grant A0102A07178) and CALMIP (Grant 2021-p1425) for providing HPC resources.

Declaration of conflicting interests

The author(s) declared no potential conflicts of interest with respect to the research, authorship, and/or publication of this article.

Funding

The author(s) received no financial support for the research, authorship, and/or publication of this article.

ORCID iDs

Dhanush Vittal-Shenoy  <https://orcid.org/0000-0002-3184-0737>

Marc C. Jacob  <https://orcid.org/0000-0001-5946-6487>

References

1. Gutin L. On the sound of a rotating airscrew. *Z Tech Fiz* 1936; 6: 889–909.
2. Leverton JW and Taylor FW. Helicopter blade slap. *J Sound Vibration* 1966; 4(33): 345–357. DOI: [10.1016/0022-460X\(66\)90132-5](https://doi.org/10.1016/0022-460X(66)90132-5)
3. Lawson MV. *Helicopter Noise: Analysis-Prediction and Methods of Reduction*, 1973. AGARD Report LS-63
4. Hanson DB. Near-field noise of high tip speed propellers in forward flight. In: 3rd Aero-Acoustics Conference, 20 July 1976–23 July 1976, Palo Alto, CA.
5. Grande E, Romani G, Ragni D, et al. Aeroacoustic investigation of a propeller operating at low reynolds numbers. *AIAA J* 2021; 09: 1–12. DOI: [10.2514/1.j060611](https://doi.org/10.2514/1.j060611)
6. Gojon R, Jardin T and Parisot-Dupuis H. Experimental investigation of low reynolds number rotor noise. *The J Acoust Soc America* 2021; 149(6): 3813–3829. DOI: [10.1121/10.0005068](https://doi.org/10.1121/10.0005068)
7. Romani G, Grande E, Avallone F, et al. Computational study of flow incidence effects on the aeroacoustic of low blade-tip Mach number propellers. *Aerospace Sci Tech* 2021; 120: 107275. DOI: [10.1016/j.ast.2021.107275](https://doi.org/10.1016/j.ast.2021.107275)
8. Moreau S, Mendonca F, Qazi O, et al. Influence of turbulence modeling on airfoil unsteady simulations of broadband noise sources. In: 11th AIAA/CEAS Aeroacoustics Conference, Monterey, CA, 2005.
9. Rozenberg Y, Roger M and Moreau S. Effect of blade design at equal loading on broadband noise. In: 12th AIAA/CEAS Aeroacoustics Conference (27th AIAA Aeroacoustics Conference). Cambridge, MA, 2006.
10. Golubev V. Recent advances in acoustics of transitional airfoils with feedback-loop interactions: a review. *Appl Sci* 2021; 11(3): 1057. DOI: [10.3390/app11031057](https://doi.org/10.3390/app11031057)

11. Paterson RW, Vogt PG, Fink MR, et al. Vortex noise of isolated airfoils. *J Aircraft* 1973; 10(5): 296–302. DOI: [10.2514/3.60229](https://doi.org/10.2514/3.60229)
12. Tam CK. Discrete tones of isolated airfoils. *The J Acoust Soc America* 1974; 55(6): 1173–1177. DOI: [10.1121/1.1914682](https://doi.org/10.1121/1.1914682)
13. Arbey H and Bataille J. Noise generated by airfoil profiles placed in a uniform laminar flow. *J Fluid Mech* 1983; 134: 33–47. DOI: [10.1017/S0022112083003201](https://doi.org/10.1017/S0022112083003201)
14. Yakhina G. Experimental study of the tonal trailing-edge noise generated by low-Reynolds number airfoils and comparison with numerical simulations. *Ecole Centrale de Lyon PhD Thesis*. 2017.
15. N’Guyen LD, Golubev V, Mankbadi RR, et al. On ladder-type structure of acoustic tones radiated by transitional airfoils. In: 23rd AIAA/CEAS Aeroacoustics Conference. Denver, CO, 5–9 June 2017.
16. Yakhina G, Roger M, Moreau S, et al. Experimental and analytical investigation of the tonal trailing-edge noise radiated by low Reynolds number airfoils. *Acoustics* 2020; 2(2): 293–329.
17. Amiet RK. Noise due to turbulent flow past a trailing edge. *J Sound Vibration* 1976; 47(3): 387–393. DOI: [10.1016/0022-460X\(76\)90948-2](https://doi.org/10.1016/0022-460X(76)90948-2)
18. Howe MS. The influence of vortex shedding on the generation of sound by convected turbulence. *J Fluid Mech* 1976; 76(4): 711–740. DOI: [10.1017/S0022112076000864](https://doi.org/10.1017/S0022112076000864)
19. Moreau S, Roger M and Christophe J. Flow features and self-noise of airfoils near stall or in stall. In: 15th AIAA/CEAS Aeroacoustics Conference (30th AIAA Aeroacoustics Conference), Miami, FL, 11–13 May 2009.
20. Turner JM and Kim JW. Aerofoil dipole noise due to flow separation and stall at a low Reynolds number. *Int J Heat Fluid Flow* 2020; 86: 108715.
21. Lowson M, Fiddes S and Nash E. Laminar boundary layer aero-acoustic instabilities. In: 32nd Aerospace Sciences Meeting and Exhibit, Reno, NV, 10–13 January 1994.
22. Desquesnes G, Terracol M and Sagaut P. Numerical investigation of the tone noise mechanism over laminar airfoils. *J Fluid Mech* 2007; 591: 155–182. DOI: [10.1017/S0022112007007896](https://doi.org/10.1017/S0022112007007896)
23. Tam CK and Ju H. Aerofoil tones at moderate Reynolds number. *J Fluid Mech* 2012; 690: 536–570. DOI: [10.1017/jfm.2011.465](https://doi.org/10.1017/jfm.2011.465)
24. Nguyen L, Golubev V, Mankbadi R, et al. Numerical investigation of tonal trailing-edge noise radiated by low Reynolds number airfoils. *Appl Sci* 2021; 11(5): 2257. DOI: [10.3390/app11052257](https://doi.org/10.3390/app11052257)
25. Grebert A, Bodart J and Joly L (2016). Investigation of wall-pressure fluctuations characteristics on a NACA0012 airfoil with blunt trailing edge. In: 22nd AIAA/CEAS Aeroacoustics Conference, Lyon, France, 30 May–1 June, 2016.
26. Galbraith M and Visbal M. Implicit large eddy simulation of low Reynolds number flow past the SD7003 airfoil. In: 46th AIAA aerospace sciences meeting and exhibit. Reno, NV, January 2008.
27. Carton de Wiart C and Hillewaert K. DNS and ILES of transitional flows around a SD7003 using a high order discontinuous Galerkin method. In: *Seventh International Conference on Computational Fluid Dynamics*. Hawaii: Big Island, 2012.
28. Pope SB. Ten questions concerning the large-eddy simulation of turbulent flows. *New J Phys* 2004; 6(1): 1–35. DOI: [10.1088/1367-2630/6/1/035](https://doi.org/10.1088/1367-2630/6/1/035)
29. Pope SB. *Turbulent flows*. Cambridge University Press, 2000.
30. Skarolek V and Miyaji K. Transitional flow over a SD7003 wing using flux reconstruction scheme. In: 52nd Aerospace Sciences Meeting National Harbor, National Harbor, Maryland, 13–17 January 2014.
31. Garmann DJ and Visbal MR. High-order solutions of transitional flow over the SD7003 airfoil using compact finite-differencing and filtering. In: *1st International Workshop on High-Order CFD Methods*, 2012.
32. Sutton D. *Experimental Characterization of the Effect of Freestream Turbulence Intensity on the SD7003 Airfoil at Low Reynolds Numbers*. PhD thesis, 2015.

33. Tank J, Smith L and Spedding GR. On the possibility (or lack thereof) of agreement between experiment and computation of flows over wings at moderate Reynolds number. *Interf Focus* 2017; 7(1): 20160076.
34. Jacob MC, Boudet J, Casalino D, et al. A rod-airfoil experiment as benchmark for broadband noise modelling. *J Theoret Comput Fluid Dyn* 2005; 19(3): 171–196.
35. Boudet J, Grosjean N and Jacob MC. Wake-airfoil interaction as broadband noise source: a large-eddy simulation study. *Int J Aeroacoustics* 2005; 4(1): 93–116. DOI: [10.1260/1475472053730093](https://doi.org/10.1260/1475472053730093)
36. Towne A, Schmidt OT and Colonius T. Spectral proper orthogonal decomposition and its relationship to dynamic mode decomposition and resolvent analysis. *J Fluid Mech* 2018; 847: 821–867. DOI: [10.1017/jfm.2018.283](https://doi.org/10.1017/jfm.2018.283)
37. Schmidt OT, Colonius T, Na Y, et al. Guide to spectral proper orthogonal decompositionThe structure of wall-pressure fluctuations in turbulent boundary layers with adverse pressure gradient and separation. *AIAA JJ Fluid Mech* 2020; 12377: 4013347–4041373.
38. Na Y and Moin P. (1998). The structure of wall-pressure fluctuations in turbulent boundary layers with adverse pressure gradient and separation. *Journal of Fluid Mechanics*, 377, 347-373. DOI: [10.1017/S0022112098003218](https://doi.org/10.1017/S0022112098003218)
39. Abe H. Reynolds-number dependence of wall-pressure fluctuations in a pressure-induced turbulent separation bubble. *J Fluid Mech* 2017; 833: 563–598.
40. Wu W, Meneveau C and Mittal R. Spatio-temporal dynamics of turbulent separation bubbles. *J Fluid Mech* 2020; 883: A45. DOI: [10.1017/jfm.2019.911](https://doi.org/10.1017/jfm.2019.911)
41. Viaro S and Ricco P. Compressible unsteady görtler vortices subject to free-stream vortical disturbances. *J Fluid Mech* 2019; 867: 250–299.
42. Désert T, Jardin T, Bézard H, et al. Numerical predictions of low reynolds number compressible aerodynamics. *Aerospace Sci Tech* 2019; 92: 211–223. DOI: [10.1016/j.ast.2019.05.064](https://doi.org/10.1016/j.ast.2019.05.064)
43. Munday PM, Taira K, Suwa T, et al. Nonlinear lift on a triangular airfoil in low-reynolds-number compressible flow. *J Aircraft* 2015; 52(3): 924–931.
44. Panda J, Raman G, Zaman KBMQ, et al. Underexpanded screeching jets from circular, rectangular and elliptic nozzles. In 3rd AIAA/CEAS Aeroacoustics Conference, 12–14 May 1997, Atlanta, GA, 1997.